Performance of a complementary metal-oxide-semiconductor sensor for laser guide star wavefront sensing

Zibo Ke, Felipe Pedreros Bustos, Jenny Atwood, Anne Costille, Kjetil Dohlen, El Hadi, Jean-Luc Gach, Glen Herriot, Zoltan Hubert, Pierre Jouve, et al.

Performance of a complementary metal-oxide-semiconductor sensor for laser guide star wavefront sensing

Zibo Ke[a,†], Felipe Pedreros Bustos[a,†], Jenny Atwood[b], Anne Costille[a], Kjetil Dohlen[a], Kacem El Hadi[a], Jean-Luc Gach[a], Glen Herriot[b], Zoltan Hubert[c], Pierre Jouve[a], Patrick Rabou[c], Jean-Pierre Veŕan[b], Lianqi Wang[d], Thierry Fusco[e,a], Benoit Neichel[a]

[a]Aix Marseille Univ, CNRS, CNES, LAM, Marseille, France
[b]NRC-Herzberg Astronomy & Astrophysics, Canada
[c]Univ. Grenoble Alpes, IPAG, CNRS, France
[d]TMT International Observatory LLC
[e]DOTA, ONERA, Université Paris Saclay (COmUE), Châtillon, France

Abstract. The adaptive optics (AO) systems of future Extremely Large Telescopes (ELTs) will be assisted with laser guide stars (LGS) which will be created in the sodium layer at a height of $\approx$ 90 km above the telescopes. In a Shack-Hartmann wavefront sensor, the long elongation of LGS spots on the sub-pupils far apart from the laser beam axis constraints the design of the wavefront sensor (WFS) which must be able to fully sample the elongated spots without undersampling the non-elongated spots. To fulfill these requirements, a newly released large complementary metal oxide semiconductor (CMOS) sensor with 1100×1600 pixels and 9 μm pixel pitch could be employed. Here, we report on the characterization of such a sensor in terms of noise and linearity, and we evaluate its performance for wavefront sensing based on the spot centroid variations. We then illustrate how this new detector can be integrated into a full LGS WFS for both the ESO ELT and the TMT.

Keywords: CMOS detector, Wavefront sensing, Extremely Large Telescopes, ELT, TMT, Laser Guide Stars.

† co-first authors. Send all correspondence to felipe.pedreros@lam.fr

Accepted for publication in SPIE Journal of Astronomical Telescopes, Instruments, and Systems on Apr. 14, 2022.

1 Introduction

The astronomical community has just launched the construction of the largest ground-based telescopes, with the European Southern Observatory's Extremely Large Telescope (ESO ELT) and its primary mirror of 39 m in diameter on one hand, and the Thirty Meter Telescope (TMT) and its 30 m primary mirror on the other hand. These telescopes will answer fundamental questions ranging from the detection and characterization of exoplanets[1] to the formation and evolution of the first galaxies of the universe.[2] In order to achieve their scientific goals, the TMT and the ESO ELT require the use of adaptive optics (AO) to compensate for the aberrations introduced by atmospheric turbulence in the wavefront of the objects under study.[3] An AO system needs a bright star within the field of view of observation to measure the wavefront distortions using a wavefront sensor (WFS), typically a Shack-Hartmann WFS. These distortions are corrected in real-time by applying a feedback signal into a deformable mirror located in the optical path of the telescope, resulting in a flattened wavefront and therefore a near diffraction-limited image delivered to the science instrument. If a bright natural star is not available, an artificial beacon (laser guide star or LGS) is created by means of optical excitation of a layer of sodium atoms between 85 km and 100 km in altitude using one or several lasers launched from the telescope.[4,5] The light emitted from the LGS is then used as a reference for the WFS in the AO system.

Laser excitation of the sodium layer produces a long column of fluorescent atoms whose extension depends on the pointing angle of the telescope and the vertical density profile of the sodium layer. For an observer located only a few meters off-axis from the laser launch telescope (LLT), the LGS appears as an elongated object instead of a point source. The LGS spot elongation becomes dramatic for a 39 m-class telescope with side LLT configuration as the ESO ELT.[6] For example, the LGS produced by a 30 cm laser beam projected at zenith, will be seen by the sub-aperture of a Shack-Hartmann WFS opposite to the LLT on a 39 m diameter telescope as an elongated spot of about 10–20 arcsec long and about 1 arcsec width. The situation is less dramatic for the TMT, as it uses a central launch scheme, reducing the expected elongation by a factor $\approx$2 compared with the configuration of the ESO ELT. In all cases, the spot elongation depends on the pointing angle.

For a Shack-Hartmann WFS, the spot elongation introduces several issues. On the one hand, it reduces the signal-to-noise ratio since the same amount of photons once concentrated in a small spot are now distributed on a larger area on the detector, and on the other hand, it increases the wavefront error due to the growing uncertainty in the estimation of the center of gravity (CoG) of an elongated spot.[7] In addition, the spot truncation due to highly elongated spots not completely imaged on a given sub-aperture, leads to a bias in the estimation of the CoG in proportion to the fraction of truncation.[8]

Thus, the major challenges of LGS wavefront sensing at the ELTs scale lie on i) performing a robust wavefront analysis on a single object strongly extended and whose elongation varies across the pupil, and ii) developing a large, fast and low-noise wavefront sensor able to image the full pupil and, at the same time, provide enough sampling for both elongated and non-elongated spots. While several post-processing strategies to mitigate elongated elongated LGS have been developed,[9–14] we devote this work to the study of a recently-released complementary metal oxide semiconductor (CMOS) sensor intended to be used in a Shack-Hartmann WFS for the ESO ELT and the TMT.

In Sec. 2 we lay out the primary requirements of a LGSWFS for ELTs and give an overview of possible technological solutions. In Sec. 3 we characterize a candidate CMOS sensor for the LGSWFS. In Sec. 4 we provide an analysis of the impact of this type of sensor in wavefront sensing. In Sec. 5 we present two examples of implementation of this sensor in LGS WFS for ESO ELT and TMT. Finally, in Sec. 6 we assess our results and provide recommendations for the use of a CMOS sensor in the ongoing design of LGSWFS.

2 A detector for LGS wavefront sensing

2.1 Requirements for ELTs

To guarantee a correct measurement of the incident wavefront, the telescope pupil must be spatially sampled with a constant pitch of about 50 cm on the primary mirror. Taking as example the 39 m diameter telescope of the ESO ELT, the Shack-Hartmann wavefront sensor needs to accommodate at least 78$\times$78 sub-pupils.

In a linear regime the LGS spots must be sampled at the accepted Nyquist sampling criteria of 2 pixels per FWHM. The minimum size of the LGS spot seen by the WFS depends on a number of factors like the laser beam size, telescope altitude, zenith angle, seeing, and thickness of the sodium layer. Statistical analysis of the LGS spot size at Paranal, shows a median angular spot size in the non-elongated direction of 1.5 arcsec FWHM and as low as of 0.95 arcsec FWHM in good atmospheric conditions.[15,16] Taking an LGS spot size of 1.0 arcsec, a pixel scale of 0.5 arcsec/pixel is required to fulfill the Nyquist criteria. Furthermore, if we consider a spot elongation of 16 arcsec

on the outermost sub-pupils (this is the case for a ≈20 km vertical thickness sodium layer and a pointing angle of 30°), then a total of ≈32×32 pixels per sub-pupil are needed to avoid truncation of the spot in the vertical or horizontal direction. To first order, a wavefront sensor with a full size of at least 2496×2496 pixels would be necessary to sample the ESO ELT pupil using 78 sub-pupils across and avoiding truncation of the elongated spot while keeping the non-elongated direction sampled within the Nyquist criteria. Following a similar approach, the TMT configuration would require a wavefront sensor with 960×960 pixels.

The minimum required photon return flux of an LGS generated with state-of-the-art 20 W lasers is near 4×10^6 photons/s/m^2, therefore the photon flux in a square sub-pupil of 50 cm side length is on the order of 1×10^6 photons/s. Given the nominal integration time of 2 ms (500 Hz) required for AO correction, and provided an estimated optical throughput of 35%, the number of photons per frame on a single sub-aperture of the WFS is ≈ 700 photons. The detection signal-to-noise-ratio (SNR) can be expressed as

$$\mathrm{SNR} = \frac{N_P \times \mathrm{QE}}{\sqrt{N_P \times \mathrm{QE} + n_{\mathrm{pix}} \times \mathrm{RON}^2}}, \tag{1}$$

where N_P is the number of photons per sub-aperture per frame, QE is the quantum efficiency of the detector, RON is the root-mean-squared (RMS) read-out noise in electrons/pixel/frame, and n_{pix} is the number of pixels used to sample the LGS spot. Assuming $N_P = 700$ photons, QE $= 0.7$, $n_{\mathrm{pix}} = 4$, and RON $= 3$ e$^-$/pixel/frame, we get an SNR of 21 for the case of a non-elongated spot. Considering an elongated spot covering 16 arcsec, we require $n_{\mathrm{pix}} = 2 \times 32 = 64$ pixels for which we get an SNR of 15. At this point, we approach the read-out-noise-limited regime and, for example, doubling read-out noise (RON $= 6$ e$^-$/pixel/frame) gives an SNR of 9 for the same elongated spot. Therefore, it is critical that the read-out noise of the sensor used for the Shack-Hartmann WFS be as low as possible.

This example shows that an adequate detector for LGS wavefront sensing requires a) a large number of pixels, b) to operate at fast frame rates, and c) to have a very low read-out noise, as specified before. Such a detector has not yet being developed as it is beyond the current technological capabilities, hence the final design of the wavefront sensor is constrained to the availability of existing detectors that can partially or in full, satisfy the aforementioned requirements.

Different technological strategies have been followed to try to answer this challenge. On the one hand, dedicated custom detector developments have been proposed both for the TMT and the ESO ELT. For the former, the idea was to exploit the specific geometry of the LGS spots, and a radial charge-coupled device (CCD) has been proposed to fit the spot elongations.[17] Indeed, due to the central launch configuration, the spots seen by each of the LGSWFS Shack-Hartmann will be radially oriented. The proposed design implemented sub-apertures of about 4×16 pixels, with a radial geometry adapted to the spot elongation. For the ESO ELT, a custom technological development toward a large 1600×1600 pixels sensor was also attempted,[18] resulting in a 800×800 pixels detector (Large Visible adaptive optics Sensor Module, LVSM).[19] In this paper we explore an alternative route offered by CMOS detectors, potentially offering large arrays, with low-noise and high frame-rate.

2.2 *CMOS technology for LGS wavefront sensing*

CMOS detectors are becoming competitive with respect to traditional CCD for astronomical detection. The construction design of CCDs in which there is only one or few read-out amplifiers for the whole array, increases the overall detector latency as the charge from each pixel are read out sequentially through the amplifiers. In contrast, CMOS technology has one read-out amplifier per pixel allowing massive parallel readout through read-out buses, hence reducing the latency of the sensor array. There are several ways to implement this process across the whole 2D array. Classically, the sensor can be read line-by-line which is known as rolling shutter architecture. This architecture has the advantage to use only a few transistors per pixel (3 or 4) leading to simpler and lower noise CMOS imagers. However, each line of the array is exposed and read out sequentially so at different instants across the whole array. For objects moving at speeds comparable with the frequency of read-out, the images acquired with a rolling shutter sensor exhibit a distortion artifact called jelly effect. This is a potential disadvantage for wavefront sensing, because of the WFS may not be able to capture the state of the turbulence during one frame without introducing temporal shifts over the pupil spots.

However, in 1997 Fossum[20] introduced a more complex architecture using 5 transistors per pixel giving the ability to take a snapshot of the scene and store it in a memory which is then read out sequentially while the next image is integrated. In this scheme all pixels are read out at different instants, but exposed for the same amount of time, hence eliminating the temporal shifts in the final image. This architecture has the drawback of high read-out noise because of the Johnson–Nyquist reset noise that remains during read out. Later, more complex architectures using 6 transistors[21] or even 8 or 11 transistors architectures[22] permitted to integrate a correlated double sampling circuitry in each pixel that subtracts the thermal noise at the expense of a much higher pixel complexity. Usually these imagers use finer lithographic pitch CMOS processes to keep the ratio of detection diode and transistor surface at an acceptable level compared to simpler architectures. The memory zone needs to be metal shielded to avoid collecting light, therefore the pixel fill factor of global shutter devices cannot reach 100% by construction, even if they are back illuminated. To overcome this limitation, micro lenses are integrated in the sensor to concentrate the light falling across the pixel on the detection diode.[23] However, this also brings a reduction in the sensor's sensitivity for oblique angle of incidence. This effect is seldom reported, but it plays an important role in the design of a wavefront sensor.

Recent developments in CMOS technology for astronomical applications[24,25] facilitated the rapid improvement in their performance that narrows or even surpass the gap with CCD. For example, the use of pinned photodiode reduces the dark current significantly,[26] and increasing the conversion gain or the implementation of source-follower transistor structures reduce read-out noise to sub-electron levels.[27] High quantum efficiency is another characteristic relevant for low-light applications, which has been addressed by using back-thinned CMOS sensors.[28] In addition to achieving high performance, another advantage of CMOS detectors is their capability to be operated at room temperature or alternatively with simple water-cooling, without the need of cryocoolers. This feature drastically reduce the complexity of the instrument.

In the following sections, we report on the characterization of a large CMOS sensor and its impact on the performance of laser guide star wavefront sensing.

3 Characterization of a CMOS sensor

3.1 Parameters

The sensor we evaluate is a Sony CMOS detector model IMX425LLJ on board of a C-BLUE One camera manufactured by First Light Imaging.[29] The detector array has 1604 $\times$ 1104 active pixels, each of which with a square size of 9.0 μm $\times$9.0 μm. The active pixels include an analog-to-digital converter of 8, 10, or 12-bits and global shutter read-out. The quantum efficiency reported by the manufacturer is 0.70 at 590 nm.

In the following we present the characterization of read-out noise, angle of acceptance and cosmetics of the CMOS sensor.

3.2 Noise characterization

The main three sources of noise in an optical sensor are the read-out noise, the photon noise, and the fixed pattern noise (FPN). Read-out noise arises from the process of reading the pixel data. Photon noise is due to the quantum fluctuations of the light source and its occurrence is characterized by a Poisson probability distribution. The FPN is caused by spatial inhomogeneities across the sensor array in the analog-to-digital converter (ADC) embedded in each pixel.

In order to characterize the noises of the sensor, the photon transfer curve (PTC) can be obtained. The PTC describes the relationship between the output signal at different flux levels and the corresponding fluctuations (standard deviation) of the output signal.[30] We assume that the total noise of the sensor in analog-to-digital units (ADU) is $\sigma_{\text{Total}}(\text{ADU})$ and it can expressed as

$$\sigma_{\text{Total}}(\text{ADU}) = [\sigma^2_{\text{RON}}(\text{ADU}) + \sigma^2_{\text{PN}}(\text{ADU}) + \sigma^2_{\text{FPN}}(\text{ADU})]^{1/2}, \tag{2}$$

where $\sigma_{\text{RON}}(\text{ADU})$ is the read-out noise, $\sigma_{\text{PN}}(\text{ADU})$ is the photon noise, and $\sigma_{\text{FPN}}(\text{ADU})$ is the fixed pattern noise.

The total noise can be obtained as the standard deviation of the average flux on a certain region in the sensor after offset subtraction. The photon noise in ADU can be expressed as

$$\sigma_{\text{PN}}(\text{ADU}) = \left[\frac{S(\text{ADU})}{K(\text{e}^-/\text{ADU})}\right]^{1/2}, \tag{3}$$

where $S(\text{ADU})$ is the average flux of the frame, and $K(\text{e}^-/\text{ADU})$ is the average conversion gain of the pixels.

The fixed pattern noise is stationary and it can be removed by taking the difference of two consecutive frames acquired with the same exposure time.[30] Then, the sum of read-out and photon noises can be expressed as

$$\sigma_{\text{RON+PN}}(\text{ADU}) = \left\{\frac{\sum_{i=1}^{N_{\text{PIX}}}[F1_i(\text{ADU}) - F2_i(\text{ADU})]^2}{2N_{\text{PIX}}}\right\}^{1/2}, \tag{4}$$

where $F1_i(\text{ADU})$ and $F2_i(\text{ADU})$ is the output signal of pixels i of two consecutive frames within a region of N_{PIX} pixels.

After removing the fixed pattern noise, we can estimate the photon noise as

$$\sigma_{\text{PN}}(\text{ADU}) = \left[\sigma_{\text{RON+PN}}(\text{ADU})^2 - \sigma_{\text{RON}}(\text{ADU})^2\right]^{1/2}. \tag{5}$$

In order to get results in electron unit, we need to obtain the gain of the pixel which can be expressed as

$$K(\mathrm{e}^-/\mathrm{ADU}) = \frac{S(\mathrm{ADU})}{\sigma^2_{\mathrm{PN}}(\mathrm{ADU})}. \tag{6}$$

The measurements to characterize the PTC were performed as follows. A fiber-coupled light-emitting-diode (LED) with central wavelength of 595 nm and linewidth of 80 nm was used as a light source. The beam out of the fiber back-illuminated a diffuse white-translucent surface placed in front of the sensor. Black tubing was used between the illuminated surface and the sensor to minimize background light. The acquisition frame rate was set as 481 Hz, the sensor temperature was 36°C. Although the light source over illuminated the full array, we only evaluated a region of 100×100 pixels in the center of the sensor array to minimize errors due to illumination inhomogeneity. Illumination and frame rate were held constant over the measurements, only varying the exposure time of the array.

The resulting PTC is shown in Fig. 1 (left). Three regions can be distinguished in the PTC: the read-out noise region at low signal level, the photon-noise region at intermediate signal, and the FPN region at high signal level. Since the read-out noise is the dominant noise source at low signal level, it can be obtained in ADU units as the noise corresponding to a signal of 1 ADU, which is found by linear fitting of the two lowest signal data points. With increasing signal, the photon noise sets in and follows a linear relationship on the log-log coordinates as shown in yellow squares and with a linear fit. At high levels of signal pixels start to saturate. The full well capacity S_{FW} characterizes the saturation point and it can be calculated by the product between the signal value in ADU at the saturation point and the gain. Then, the estimated read-out noise, full well capacity and gain are $\sigma_{\mathrm{RON}} = 3.05 \pm 0.15$ e$^-$, $K = 0.2473 \pm 0.012$ e$^-$/ADU, and $S_{\mathrm{FW}} = 931$ e$^-$, respectively.

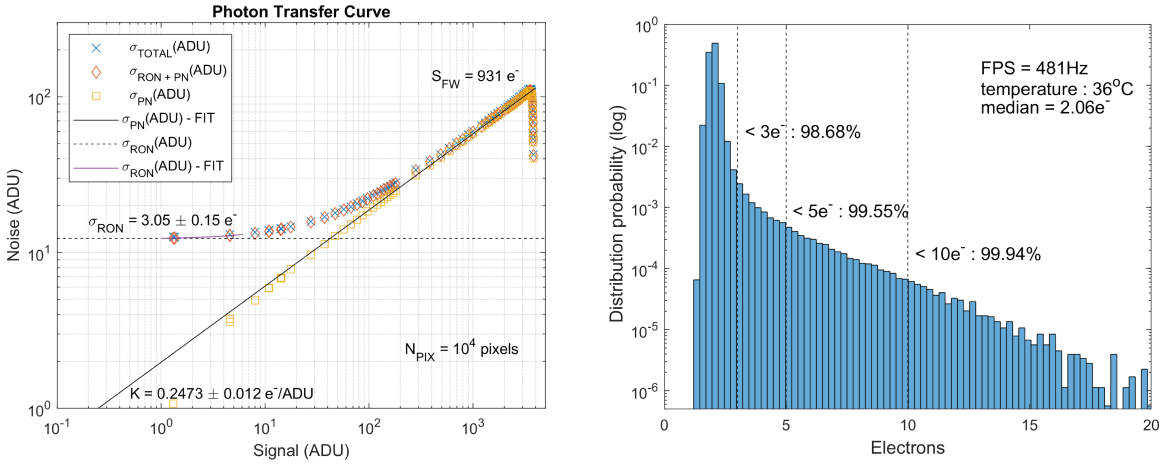

Fig 1 (Left) Measured photon transfer curve of the CMOS detector. (Right) The histogram of read-out noise.

An alternative method consists in acquiring a series of dark frames with short integration time (0.01 ms) and computing the temporal standard deviation of individual pixels. The distribution of noise over the full array is shown as the histogram in Fig. 1 (right). The median read-out noise is 2.06 e$^-$, which is consistent with the result obtained from the photon transfer curve. The tail that appears on the distribution is attributed to random telegraph noise (RTN) arising from traps at the

thin-layer interface in the source-follower gate region of metal-oxide-semiconductor field-effect transistors (MOSFET) of individual pixels.[31]

3.3 Angle of acceptance

CMOS sensors have small microlenses at the surface of their pixels that enhance their photon collection efficiency.[23,32] Although the on-axis sensitivity is improved, incident light at oblique angles is focalized off the center of the photosensitive area into light-insensitive structures of the pixel. This leads to a reduction in sensitivity for a light beam with a large angle of incidence. The characterization of the angle of acceptance is critical for the optical design of the wavefront sensor as it allows choosing the appropriate beam F-ratio that minimizes the detection losses.

The measurements setup is described as follows. The output beam from a fiber-coupled LED source (595 nm central wavelenght, 80 nm FWHM linewidth) is collimated with a 100 mm lens to a 23 mm diameter beam. A filter of 10 nm FWHM width centered at 590 nm is used to narrow the spectral width of the source around the sodium emission wavelength. A pupil of 4.2 mm clips the beam that is imaged with a 1:1 lens system into the center of the sensor plane. The sensor is mounted on a micrometric stage that allows on-axis and horizontal rotation. For an initial on-axis position, the sensor is rotated $\pm 26^\circ$ in the horizontal plane. A sequence of 100 frames is obtained for each angular position. The resultant average of the 100 frames is calculated. A window of 100×100 pixels centered in the circular footprint of the beam is used for processing. The average of all pixels in the window is taken as the representative intensity of the pixels. Due to the reducing irradiance on the sensor with increasing angle (the beam becomes elliptical on the sensor plane for large incidence angles), a factor of $1/\cos(\gamma)$ is applied to the normalized intensity values, where γ is the tilt angle of the sensor plane. After the full horizontal range is measured, the sensor plane is rotated in the optical axis and a new series of measurements are taken by rotating the sensor around the horizontal plane. Repeating this process, a complete angular sensor response is characterized.

Figure 2 shows the normalized response of the sensor in eight transverse planes. In the same figure, a contour plot representation of the angular response is shown. The response of the sensor is maximal at 0° incidence and decreases for larger angles. For each plane, the angular response is

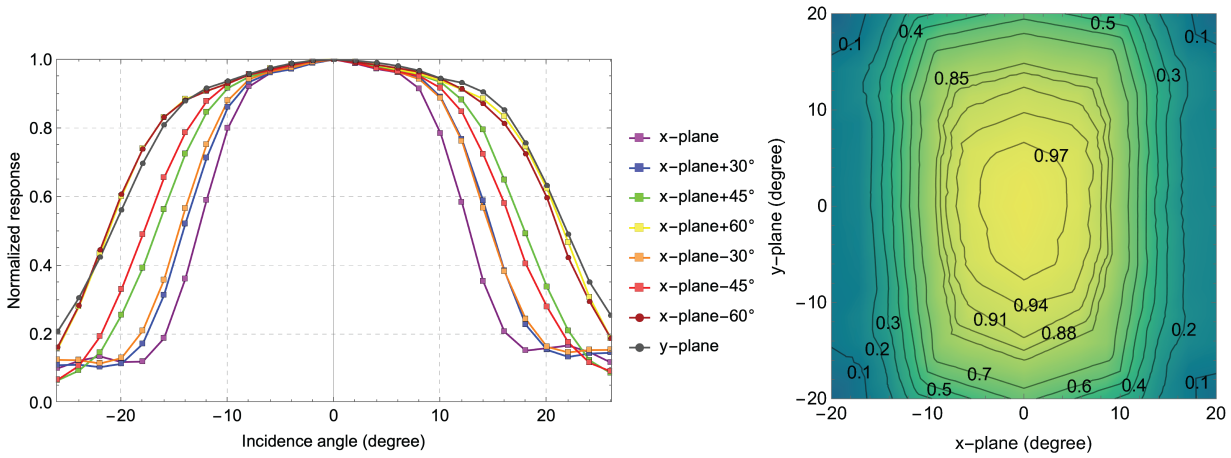

Fig 2 (Left) Normalized pixel angular response of CMOS detector in eight transverse planes (Right) Contour plot of the averaged-normalized angular pixel response.

symmetric around the normal, but the acceptance angle is wider in the vertical direction. This could be explained by the presence of a rectangular photosensitive area elongated across the vertical axis.

Any systematic mismatch between the microlenses and the pixels would result in a tilt of the acceptance direction. In addition to the measurements presented in Fig. 2, we measured the angular response on 100×100 pixels windows located at the edges of the sensor in the x and y planes, showing no difference among them in the direction of maximum efficiency nor in the angular width. This indicates that the angle of acceptance is homogeneous over the sensor.

We will show in section 4.3 how the angle of acceptance leads to light losses as a function of the focal ratio of the incident beam on the detector.

3.4 Cosmetic

Because the size of the spot on the wavefront sensor is near a single pixel within the subaperture, it is crucial that the sensor array is free of defective elements (also called cosmetic defects). Hot (bright) or cold (dark) pixels in a subaperture would cause a bias in the centroiding calculation, or a complete loss of the measurement if the defective pixel is located within the LGS spot.[33] Other cosmetic defects may include pixels with temporal instability and non-linear behaviour.

To characterize the presence of defective pixels we take a flat illuminated image with mean intensity at half the full-well-capacity, and we calculate the histogram (Fig. 3). We found no dark nor bright pixels over the entire array, which rules out any loss in performance due to defective elements.

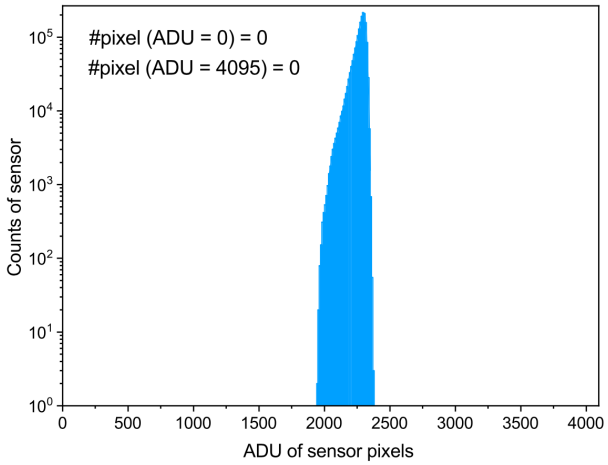

Fig 3 Logarithmic histogram of the flat illuminated image. No dead nor hot pixels are found.

4 Impact on LGS WFS

4.1 Centroiding error

The main sources of noise present in a wavefront sensor are photon noise and read-out noise. These two sources of noise can be expressed as two additive terms in the error of the center-of-gravity (CoG) estimator according to:[34]

$$\sigma^2_{\text{CoG}} = \underbrace{\frac{N_T^2}{8\ln(2)S_e}}_{\text{Photon}} + \underbrace{\left(\frac{\sigma_{\text{RON}}}{S_e}\right)^2 \cdot \left(\frac{N_S^4}{12}\right)}_{\text{Read-out}}, \tag{7}$$

where N_T is the full width at half maximum (FWHM) of the spot on the image, N_S is the side length of the sub-aperture in pixels, σ_{RON} is the read-out noise, and S_e is the number of photons per sub-aperture and per frame.

Similarly, the weighted CoG (WCoG) can be expressed as:[35]

$$\sigma^2_{\text{WCoG}} = \underbrace{\frac{N_T^2}{8\ln(2)S_e} \cdot \left(\frac{N_T^2 + N_W^2}{2N_T^2 + N_W^2}\right)^2}_{\text{Photon}} + \underbrace{\frac{\pi(N_T^2 + N_W^2)^2}{128(\ln(2))^2} \cdot \left(\frac{\sigma_{\text{RON}}}{S_e}\right)^2}_{\text{Read-out}}, \tag{8}$$

where N_W is the FWHM of a weighted gaussian function. We compare the theoretical centroiding error using the expressions above versus simulated and measured center-of-gravity errors. Figure 4 shows the CoG and WCoG variance as a function of the input flux. Dashed lines show the photon-noise and read-out-noise components of the theoretical centroiding variance according to equations 7 and 8. We assumed $\sigma_{\text{RON}} = 2.06\ \text{e}^-$, as measured previously. Using $N_S = 5$ pixels and $N_W = 4$ pixels, read-out noise dominates the centroiding error in the low-flux regime below $\approx 4\times 10^2$ (photons/sub-aperture/frame) in the case of CoG estimation, and below $\approx 2\times 10^2$ (photons/sub-aperture/frame) for WCoG. The solid-blue line is the total variance of the CoG estimators. The green and orange squares are simulated centroiding errors. A gaussian spot of FWHM $= 1.5$ pixels was simulated on a 13×13 pixels sub-aperture. Photon noise was added to the simulated spot, as well as read-out noise following the skewed distribution shown in Fig. 1. The centroids of 500 simulated spots were estimated for each flux level using the CoG and WCoG methods. The simulated data points in the figure show the temporal variance in the x and y direction of the sequence. In addition, centroiding measurements were performed by focalizing a spot of FWHM $=$ 1.5 pixels at the center of the sensor. The width was estimated by a gaussian fit on the measured spot. A sequence of 500 frames with 2 ms integration time was obtained for each flux level, and the variance of the CoG sequence was calculated which corresponds to the centroiding error shown in Fig. 4. There is a good agreement between the simulated errors and the measurements, and a reasonable agreement with the theoretical curves. The WCoG is able to reduce the centroiding error by a factor of ≈2 at a nominal flux of 1000 (photons/subaperture/frame).

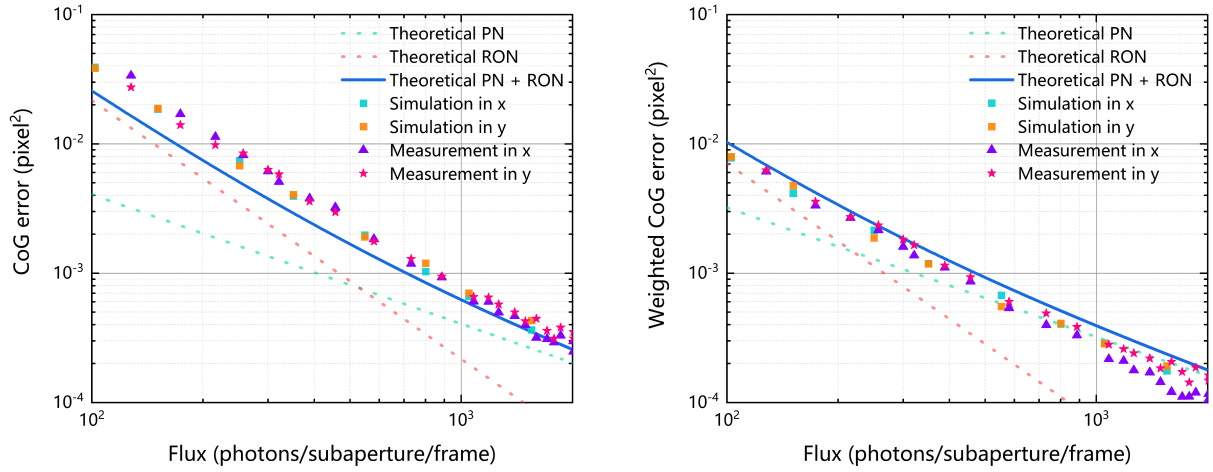

Fig 4 (Left) Comparison of error variance of CoG among real measurements, simulation and theory. (Right) Comparison based on weighted CoG.

In the case of elongated spots the centroiding error scales with the spot FWHM (N_T), and the size of the window or the shape of the weighted gaussian function (as in the case of the WCoG) would have to be adapted for each spot geometry on each sub-aperture. A reasonable strategy would be to adjust the size of the weighting function to follow the elongation geometry, which should minimize the centroiding noise. In this case, Eqs. 7 and 8 remain valid along the two axes of the elongated spot, but should be scaled in proportion to the growth of the spot in the pupil along the radial direction aligned with the laser launch position.

The effect of the measured read-out noise in the centroiding is shown in Fig. 5. Here, we compare the resulting centroid error as a function of the photon flux (based on the simulations described above) for a theoretical Gaussian RON distribution and for the measured RON distribution (see inset plot). The fraction of pixels with RON higher than a theoretical Gaussian with equal median value is 1.8%. The additional error introduced by the skewed RON distribution accounts for a factor of <2 for incoming flux above 500 (photons/subaperture/frame) in the CoG and WCoG estimation.

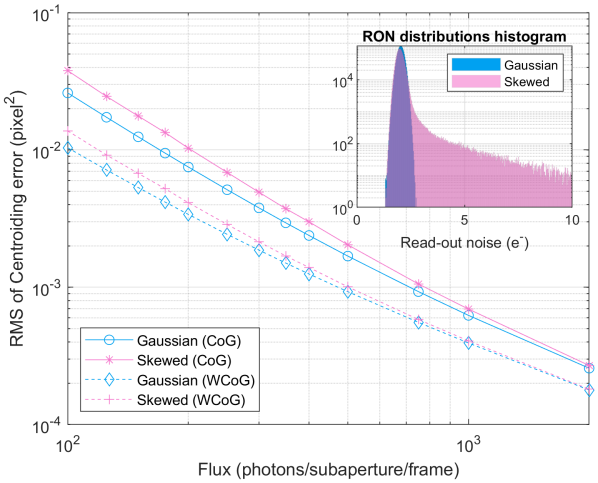

Fig 5 Centroiding error based on a theoretical Gaussian distribution of read-out noise and measured skewed distribution of read-out noise.

4.2 CoG linearity

The spot size relative to the dimensions of the pixels, i.e. the spot sampling frequency (s), can have a significant impact in the linearity of the centroid estimation as the spot size approaches the size of a pixel. Even at the accepted Nyquist sampling criteria of $s = 2$ pixel per FWHM, centroid non-linearities start to build up depending on the profile function on the detector.[36] Therefore, the selection of the spot sampling frequency in a wavefront sensor is a trade-off between minimum noise (small spot size) and high centroid linearity (large spot size). In this section we study how the centroid varies as a function of the sampling frequency and as a function of the lateral displacement of the spot over the CMOS sensor, and we compare with simulations.

The experimental arrangement consists of a fiber-coupled LED source with a fiber core of 400 μm placed at a distance of 1300 mm from a lens of 24 mm clear aperture and 40 mm focal length that forms an image of the source at the surface of the CMOS sensor located at 40 mm from

the lens. In this simple configuration, the magnification of the optical system is $M = 40/1300 = 0.03076$. The theoretical size of the image is 12.3 μm or 1.36 pixels. A lateral displacement of the source is also magnified in proportion to M. In the current setup, the source is laterally shifted with a step of $\delta_S = 40$ μm, corresponding to a spot lateral displacement step of $\delta_I = 1.2$ μm. We move the spot by 25.2 μm in steps of 1.2 μm over almost 3 pixels. For each step, we acquire 30 consecutive images and calculate the CoG for each frame. The average CoG relative to the initial pixel position and the standard deviation of the CoG are calculated as a function of the pixel position of the spot. In order to understand any possible effects of the acceptance angle in the linearity of the CoG, we repeat the procedure at different tilt angles of the sensor such that the CoG linearity can be evaluated for several angles of incidence.

The CoG at each angle of incidence θ and for a given spot sampling frequency s can be represented as a linear function plus an oscillating term as follows:

$$\mathrm{CoG}_{(\theta,s)}(x) = \underbrace{A\,x + B}_{\text{Linear}} + \underbrace{W_s \sin(2\pi x + \phi_x)}_{\text{Residual}}, \tag{9}$$

where x is the pixel displacement, A and B are parameters of the linear CoG response, W_s is the amplitude of CoG oscillations at a sampling frequency s, and ϕ_x is an arbitrary pixel phase.

Figure 6 shows the calculated CoG relative to the initial pixel position as a function of the pixel displacement for incidence angles between $-20°$ and $+20°$. A linear fit is estimated for each data set. The values of the slopes of the linear component of the CoG (parameter A) for all tilt angles are shown in the inset table in the same figure. The measured linear slope deviate less than 5% with respect to the ideal linear response ($A = 1$), showing a small effect on the linearity as a result of the angle of acceptance.

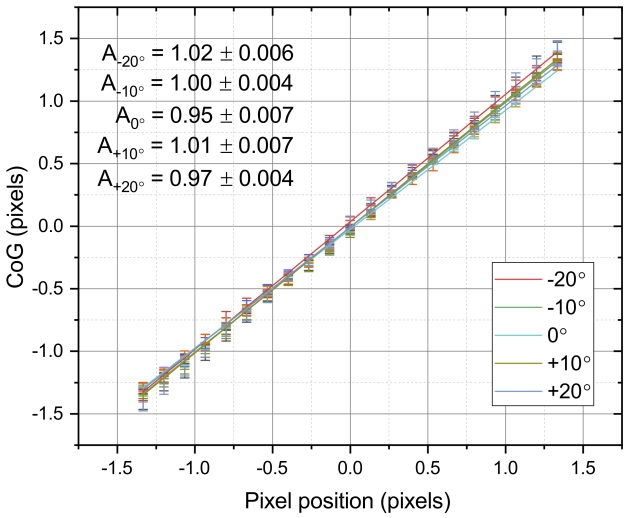

Fig 6 Measured CoG as a function of the pixel displacement with the sensor tilted at five different angles. A linear fit is applied to each data set. The spot sampling frequency was estimated as 1.13 pixels FWHM. The linear slope parameter A for each data set is shown at the top left.

Figure 7 shows the residual of the data shown in Fig. 6, i.e. the difference between the measured CoG's and the linear fit. This corresponds to the residual term of Eq. 9. We show the residuals data obtained at normal incidence and for three spot sizes: 1.10 pixel FWHM, 1.13 pixel FWHM,

and 1.34 pixel FWHM, that were obtained by slightly shifting the focal plane in the optical axis direction. The spot size are estimated using a Gaussian fit and their values correspond to the spot sampling frequency s. For each measurement, a sine function is fit to the data (blue curve) and the result of a simulation is also displayed (red curve). There is a good agreement among simulations, the fit curve, and measurements. The amplitude of the residual CoG, i.e. the degree of non-linearity, is described by the parameter W_s in Eq. 9. The value of W_s for each measurement is shown in the figure. For the most undersampled case ($s = 1.10$ pixel), the degree of non-linearity reaches 4.2% of a pixel and for the least undersampled case ($s = 1.34$ pixel) the degree of non-linearity is reduced to 1.0% of a pixel. These measurements show that the increase in CoG non-linearities in the CMOS sensor under study behave as expected, and that sampling the spot frequency below the Nyquist criteria yield a degree of non-linearities that is relatively small compared to the pixel size. Note that in the case of elongated spots, as expected for ELTs, the sampling will be different along the short and long axes of the spots. The conditions reproduced here correspond to the worst case expected for the short axis. In the elongation direction, the sampling of the spot will likely be above the Nyquist criteria, hence the linearity error vanishes.

The estimated spot size and the linearity response include any cross-talk effect between adjacent pixels, however, we assume that cross-talk is negligible (<1%) based on studies performed on a similar CMOS sensor[37] and the fact that microlenses minimize this effect.

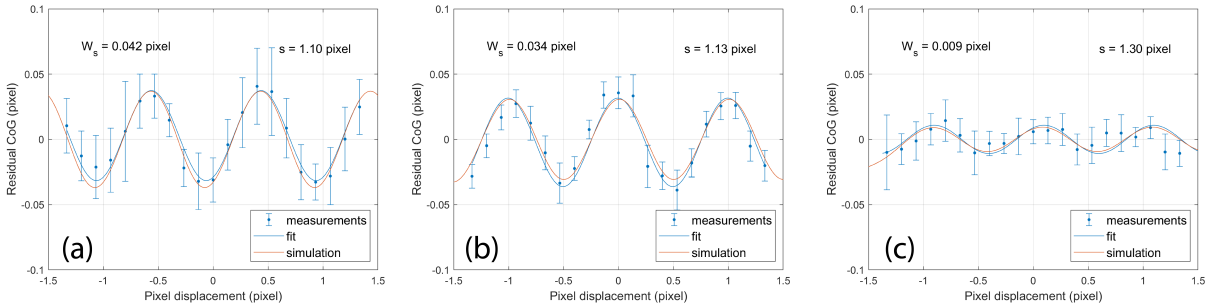

Fig 7 Residual CoG as a funcion of the pixel displacement compared to a sine fit function and simulations for a spot sampling frequency of (a) 1.10 pixels FWHM, (b) 1.13 pixel FWHM and (c) 1.34 pixel FWHM. All measurements obtained at normal incidence.

4.3 Transmission loss due to angle of acceptance

The angular response characteristic of the CMOS sensor gives rise to a transmission loss through the focalizing element (e.g. lenslet array of the Shack-Hartmann wavefront sensor) as off-axis rays are focalized into the sensor with a slanted angle of incidence.

The photon flux transmission due to the angle of acceptance can be estimated as:

$$\eta_{\text{acc}} = \frac{\int_{-\alpha}^{+\alpha}\int \hat{G}(x,y)dxdy}{H(\alpha)}, \tag{10}$$

where $\hat{G}(x,y)$ is an estimate of the normalized angular response obtained with interpolation of the

measured data over the horizontal and vertical angular directions (see Fig. 2), $H(\alpha)$ is a function that describes the lenslet window seen from the detector, and α is the beam detector angle given by

$$\alpha = \frac{1}{M} \arctan\left[\left(\frac{\epsilon+1}{2}\right)\frac{1}{2F_\ell}\right], \tag{11}$$

where F_ℓ is the lenslet nominal side F-number, $\epsilon \leq 1$ is the linear fill factor of the lenslet array, and M is the magnification of any optical relay between the lenslet array and the sensor plane. The beam F-number on the detector side is $F_d = 1/(2\ \tan(\alpha))$. For the case of a square lenslet $H_{\text{square}}(\alpha) = 4\alpha^2$ and for the case of a circular lenslet $H_{\text{circular}}(\alpha) = \pi\alpha^2$. These expressions assume no loss between the lenslet array and the detector other than the detector angular response. We also assume image telecentricity, i.e. the chief rays are always at normal incidence on the detector, independent of the position of the lenslet over the pupil and of the distance of the object from the center of the field of view.

Assuming $\epsilon = 1$ (no apodization in the lenslet array) and the measured angular response of the CMOS sensor, we estimate the transmission through a Shack-Hartmann wavefront sensor as a function of the detector F-number for the case of a circular and square lenslet configuration, as shown in Fig. 8. A reduction in transmission of 4% and 6% occurs at $f/3.0$ for the circular and square lenslet, respectively. Smaller beam F-ratios lead to a stronger reduction in transmission as the beam is focalized at larger angles. This analysis shows that purely geometric considerations in the design of a Shack-Hartmann wavefront sensor with a CMOS sensor, result in light losses that should be taken into account to minimize the impact in the overall throughput of the optical system.

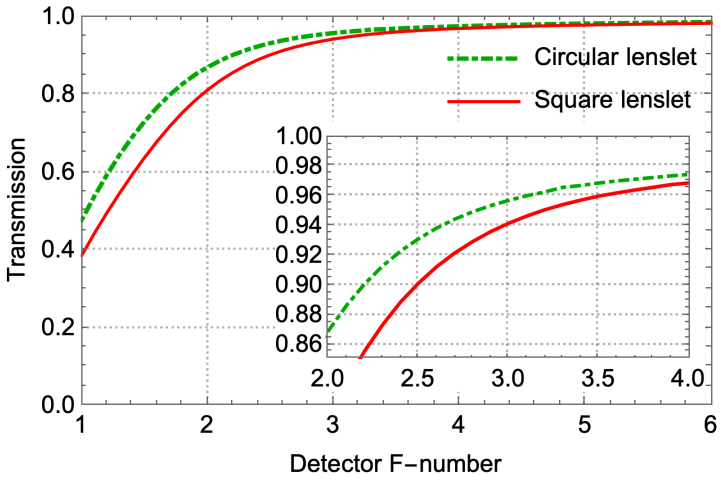

Fig 8 Transmission efficiency due to angle of acceptance of a CMOS sensor as a function of the detector side beam F-number.

5 Examples of implementation of a CMOS detector into a LGS WFS

In this section we provide a preliminary design of a full LGS WFS arm for the ESO ELT and the TMT. For the former, we take as an example the Laser Tomography Adaptive Optics (LTAO) system of HARMONI,[38] which will make use of the 6 LGS provided by the ESO ELT. For the

latter, we show the implementation for NFIRAOS,[39] the TMT Multi-Conjugate Adaptive Optics (MCAO) system. The goal of this section is not to report on a final design for the these instruments, but rather to show that a practical implementation of the CMOS sensor described in this article is feasible in LGS WFS.

5.1 HARMONI design

The main parameters of the LGSWFS for HARMONI are summarized in Table 1.

Table 1 Specifications of the HARMONI LGS WFS.

Parameter	Value	Comment
ESO ELT primary mirror diameter	39 m	Size of the pupil
# LGS	6	Side launch provided by 4 launch stations (2×2 + 2×1)
# Subaperture	68×68	Spatial sampling of 57 cm. Square lenslets.
# pixels per subaperture	16×16	with at least 15×15 useful pixels
LGSWFS pixel scale	1.1 arcsec/pixel	Required for sampling LGS spots
Subaperture Field of View	16.5 arcsec	Side FoV. Required for minimizing truncation

5.1.1 Lenslet Array

To decrease the maximum angle of arrival on the detector from LGSS, we propose to use a double lenslet concept. Figure 9 shows the ray tracing for a classical lenslet and a double lenslet[1]. The double-lenslet has the advantage of creating a telecentric image and of reducing the steepest beam angle by half. For the case of a classical lenslet placed on top of the detector, the maximum beam angle at the edge of the sub-aperture is given by

$$\theta_m^{\text{single}} = \arctan \frac{d_\ell}{f_\ell} = \arctan \frac{1}{F_\ell} \approx \frac{1}{F_\ell}, \tag{12}$$

where d_ℓ and f_ℓ are the lenslet diameter and focal length, respectively, and F_ℓ is the lenslet focal ratio. However, for a double lenslet with equal focal length on each curved face, the maximum exit beam angle from the second lenslet face (a telecentric image plane) is equal to the on-axis beam given by

$$\theta_m^{\text{double}} = \arctan \frac{d_\ell}{2f_\ell} = \arctan \frac{1}{2F_\ell} \approx \frac{1}{2F_\ell}. \tag{13}$$

The maximum beam angle in the double-lenslet configuration is one half with respect to the maximum beam angle of a single lenslet, and it is also equal for on-axis and off-axis objects, i.e. it provides the same beam angle over the full field of view (FoV).

For LTAO, a FoV of at least 16×16 arcsec^2 is required. As described above, one of the challenges imposed by the CMOS detector arises from the acceptance angle. The optical design of the lenslet array must then be carefully thought in order to minimize flux loses at the coupling with the detector.

[1] Although individual lenslets have a square geometry, we assume inscribed circular optics in the following calculations. Diagonal beam apertures are $\sqrt{2}$ faster than side beam apertures.

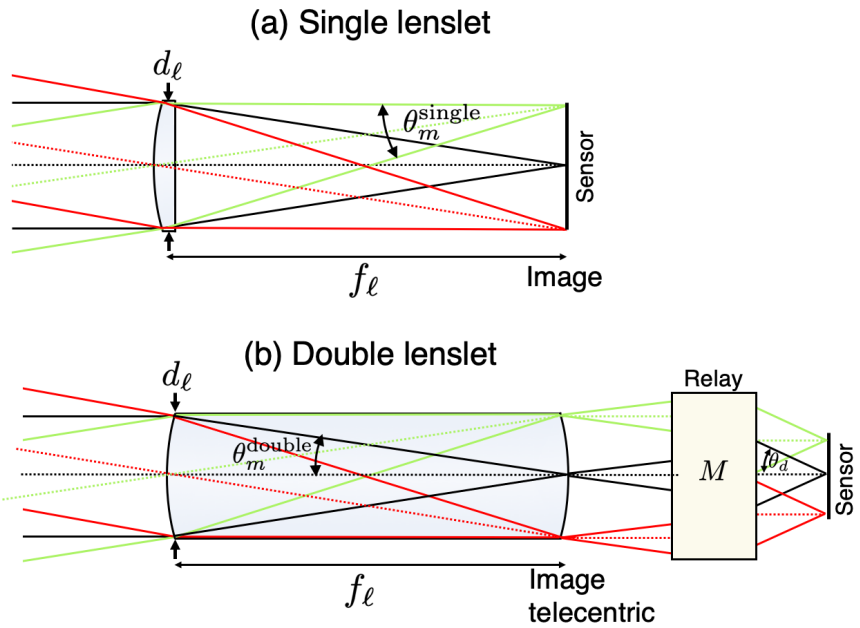

Fig 9 Schematic ray tracing comparison between (a) single lenslet in front of the detector and (b) double lenslet fabricated in the same substrate. In the double lenslet, an optical relay is required to re-image the telecentric focal plane on the detector plane. The maximum incidence angle on the sensor plane is reduced by half with respect to the single lenslet, and chief rays are parallel to the optical axis across the full FoV.

The acceptance angle is linked to the maximum focal ratio that can be accepted by the detector. The focal ratio of the beam onto the detector plane is determined by specific parameters and the following formula:

$$F_d = \frac{N \cdot d}{D \cdot \beta}, \tag{14}$$

where N is number of sub-apertures, d is the pixel size, D is the telescope pupil diameter and β is the on-sky pixel scale. For $N = 68$, $d = 9$ μm, $D = 39$ m and $\beta = 1.1$ arcsec/pixel, the detector beam focal ratio is $F_d = 2.94$ corresponding to a beam detector angle $\theta_d = 9.64°$, following the relationship $\theta_d = \arctan(1/(2F_d))$. A total of 68 sub-apertures require 1088 pixels, or 16 pixels per sub-aperture. If we consider 1 guard pixel between sub-apertures (for alignment margin purposes), there are 15 useful pixels per sub-aperture, covering a total FoV of 16.5 arcsec.

The maximum beam angle from the telecentric image plane θ_m^{double} is related to the detector beam angle θ_d as $\theta_m^{\text{double}} \approx \theta_d \cdot M$, with M the magnification of the relay. Using $M = 1/2.45$, then $\theta_m^{\text{double}} = 3.94°$ and $F_\ell = 7.27$ (Eq. 13). Considering the pupil of 24 mm and 68 sub-apertures, a double lenslet array with 353 μm lenslet pitch is required. The focal length of the lenslet can be found as $f_\ell = F_\ell \cdot d_\ell$, which gives $f_\ell = 2.57$ mm. Both powered surfaces of the double-lenslet are manufactured in the same substrate made of fused silica with index of refraction $n = 1.4584$ at 589 nm, therefore the double lenslet must have a thickness of $f_\ell \times n = 3.75$ mm.

5.1.2 Optical Relay

Due to the wide FoV required for LTAO, the focal length of a lenslet array placed in front of the detector would be very short (near 0.5 mm as it can be calculated in the previous section), which makes it technically difficult to assemble inside the detector chip. This problem is common with

other ELTs instruments, and similar conclusions apply to NFIRAOS as well. The implementation of an optical relay between the lenslet and the detector increases the overall size and the number of elements in the WFS, but it also relaxes the manufacturing complexity and tolerances of the lenslet array design. It also allows for a better management of the beam angles and acceptance within the detector. Therefore, an optical relay has three purposes: i) decouple the lenslet array focal plane from the detector focal plane, ii) reimage the telecentric image plane from the double-lenslet array at the detector plane, and iii) compress the pupil size from the lenslet array pupil to the detector size. The pupil diameter on the lenslet array is fixed to be 24 mm, due to other optical and manufacturing constraints. The pupil size on the detector is 9.792 mm, hence the magnification factor is $M = 1/2.45$. In order to provide high optical performance, both in terms of image quality and distortions, a six-lenses design has been proposed as shown in Fig. 10. The overall performance of this relay has been specified such that the distortion shall be less than ± 0.03 sub-aperture with respect to a perfect grid, with a variation of less than ± 0.01 sub-apertures within operating conditions during the instrument lifetime. In terms of optical quality, the relay does not degrade the quality of the spot image when taking onto account the quadratic sum of the contributors to the wavefront error budget. This relay also preserves the telecentricity, as this is an important factor for coupling light with detector pixels (see Section 5.1.1), and the telecentricity error is less than $\pm 1.5°$ at the detector level. Although the system contains a large number of optical surfaces, the penalty in terms of transmission budget is minor since highly efficient monochromatic anti-reflective (AR) coatings are available. High performance coatings with less than 0.25% reflectivity are considered here.

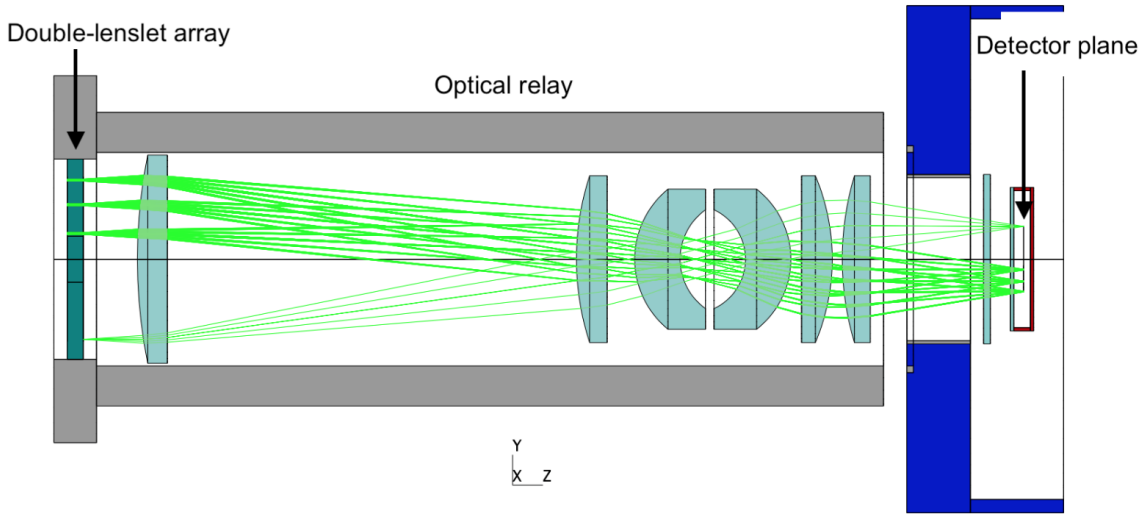

Fig 10 Ray tracing diagram of the HARMONI LGS wavefront sensor, depicting the double-lenslet array, optical relay and detector. The overall length of the relay is about 150 mm.

In summary, the HARMONI design employing a double sided lenslet array with an optical relay has several advantages:

- Reduction of the beam angle after the lenslet array.
- Creation of a telecentric image.

- Using a thick substrate of 3.75 mm, the focus of the lenslets can be on the backside of the substrate, therefore printing the same lenslet with the same focal length.
- Reduction of the size of the optics inside the relay.
- Reduction of the distortion of the relay optics.

The technical feasibility of such double lenses has been verified with industrial companies, and no issues have been identified. A prototype has been built and tested, showing the conformity of the lenslet built with HARMONI specifications.

5.2 TMT NFIRAOS design

The current baseline for NFIRAOS is provided in table 2.

Table 2 Specifications of the NFIRAOS LGS WFS.

Parameter	Value	Comment
TMT primary mirror diameter	30 m	Size of the entrance pupil
# LGS	6	Central launch provided by a single launch station
# Subaperture	75×75	Spatial sampling of 40 cm
LGS WFS pixel scale	1.0 arcsec/pixel	Required for sampling LGS spots
Subaperture Field of View	11 arcsec	Required for avoiding truncation

5.2.1 Detector configuration

One interesting feature of the CMOS detector is that the read-out architecture can be configured to skip rows. One can therefore decide to only read a region of interest (ROI), the full width of the detector, and the maximum frame rate is increased in proportion to the number of rows skipped. Since TMT has a smaller diameter and will launch its LGSs from behind the secondary mirror, NFIRAOS will see significantly less-elongated spots than HARMONI. The FoV of the NFIRAOS WFS subapertures does not need to be as large and therefore only a portion of the detector can be read. This opens a tradeoff space between the number of sub-apertures, the number of pixels per sub-aperture and the maximum frame rate.

For NFIRAOS, simulations show that a 10 arcsec sub-aperture field of view is sufficient for all simulated sodium profiles with no penalty due to truncation and a pixel scale of 1 arcsec is optimal except for very poor seeing conditions ($r_0 \approx 0.1$ m) where a larger pixel scale could provide better performance. We add one extra pixel per sub-aperture to accommodate slope offsets. It was also found that slightly over sampling the pupil with 75×75 sub-apertures, compared to the 60×60 deformable mirror (DM), helps to reduce the wavefront reconstruction error, especially in poor seeing conditions or higher signal level cases than our conservative baseline.

The minimal number of pixels required to accommodate the NFIRAOS configuration is 825×825 (11 pixels per sub-aperture over 75 sub-apertures). However, the CMOS camera will read 848×1608 pixels. The extra pixels are allocated among various optomechanical tolerances, as described in the next section.

With this design, the maximum achievable frame rate is slightly over 600 Hz which is still acceptable for the expected LGS signal levels and wind speed.

5.2.2 *ROI flexibility and tolerancing*

The WFS concept permits loosening or even avoiding various traditionally tight tolerances due to: the flexible readout region; the 23 additional pixels; and an array of 100×100 lenslets.

For example, oversampling the 60×60 DM actuator grid completely removes the strict alignment tolerances to register actuators to lenslet corners, which are usually needed for a Fried geometry. Furthermore, to handle DM pupil illumination shifts at the oversized 100×100 lenslet array, software can select an arbitrary set of lenslets. However, tolerances on magnification of the pupil image remain constrained, because sub-apertures are discretized into 11 pixels. E.g. to read 76×76 sub-apertures would require 11 rows of pixels, too large a fraction of the 23 pixel margin.

The most innovative use of the extra pixels is to handle slope offsets larger than the notional 1 arcsecond budget for non-common path aberration (NCPA) calibration. But that budget applies per sub-aperture. The square regions of pixels for each spot do not have to lie on a square grid. By adding "leap pixels" periodically between sub-apertures (Fig. 11 left), larger dynamic range of offsets can be calibrated, providing they are slowly varying across the pupil, which is the case for low-order aberrations.

One important situation is differential focus among six LGS WFSs. Time-varying global (common) distance to the sodium layer will be compensated by changing the optical path length to the WFSs via a trombone consisting of two mirrors in a V on a moving stage. However, one trombone cannot exactly compensate focus for all LGSs unless they are built and installed perfectly. Differential focus produces a different magnification of the spot pattern among the WFS, and deducts from the slope budget. However we can fix it in software by "stenciling" 11×11 pixels from the image. The stencils are chosen to always keep the slope offset within 0.5 pixel of the center.

Note that to avoid collisions between sub-aperture ROI stencils, we can only add space between them. So for e.g. astigmatism where the calibrated spot pattern is compressed in one axis and expanded orthogonally, the trombone controller calibration would be biased to always expand the pattern.

As shown in the right panel of Fig. 11, clocking of the lenslets versus the detector is handled in software. Note that because the outer active DM actuators are not in a circle, but actually a polygon with flat sides of several actuators in a line, clocking the spot pattern as shown does mean that WFS spots at vertices of the polygon do move outwards by approximately a pixel.

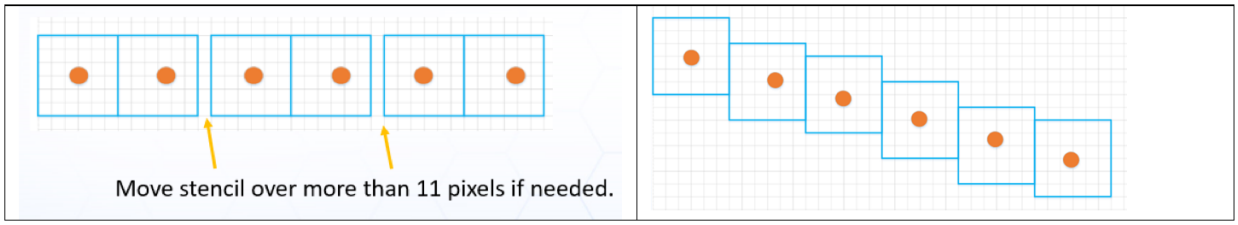

Fig 11 (Left) Leap Pixels for low order NCPA. (Right) Software defined stencils for clocking lenslets versus detector.

However, the most difficult constraint remains the profile tolerance (single digits of microns for tilts plus piston) of the detector with respect to the lenslets due to defocusing in fast beams. When NFIRAOS operates at $-30°$C thermo-mechanical analysis of the camera design indicates that the detector moves ≈ 20 μm axially towards the lens mounting interface and the optical relay shrinks in the opposite direction, compared to room temperature. We will jointly optimize the athermalization of the relay lens barrel, described below, to account for both.

5.2.3 *Lenslet array*

For NFIRAOS, we have $N = 75$, $d = 9$ μm, $D = 30$ m, $\beta = 1$ arcsec/pixel, providing a focal ratio of $F_d = 4.64$ at the detector. The steepest angle of incidence at the edge of the field of view with a conventional lenslet array would be $\theta_m^{\text{single}} = 12.2°$ resulting in light loss due to the limited acceptance angle of the CMOS pixels. This angle, and therefore the loss, would be further increased because of our proposed scheme to skip pixels in order to use larger slope offsets (section 5.2.2). This motivates the use, like HARMONI, of a double-sided lenslet array, illustrated in Fig. 9.(b) where the second surface acts as a field lens to produce a telecentric image at the detector, thus reducing the steepest angle by half. For the proposed NFIRAOS design, the main parameters of the required lenslet array are 210 μm pitch, a radius of both surfaces of 0.945 mm and thickness of 3 mm. Such a lenslet array is considered well within the capabilities of manufacturers.

5.2.4 *Optical relay*

For NFIRAOS, the pupil diameter on the lenslet array was chosen to be 15.75 mm, leading to a relay with magnification $M = 1/2$. Smaller pupil sizes make the relay shorter and therefore easier to package, but the lenslets become faster, and therefore significantly more challenging and expensive to fabricate. The 15.75 mm pupil diameter was chosen as a reasonable tradeoff.

The proposed relay is shown in Fig. 12. It has six lenses and is actually quite similar to that of HARMONI. The only possibly concerning element is the F2 lens, which exhibits a large curvature that could be costly to fabricate.

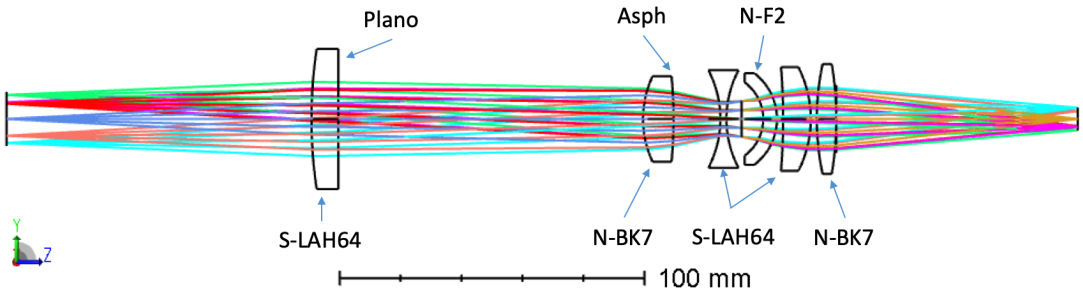

Fig 12 Ray tracing diagram of the lenslet, optical relay and detector. The overall length of the relay is about 380 mm.

This relay design has excellent image quality and distortion over the full field of view. The distortion is $<0.01\%$ and the maximum RMS wavefront error across the FoV is 0.012 waves (7 nm) with a variation of 0.005 waves. The design includes one aspheric surface on N-BK7 to help control the wavefront error at the edge of the FOV. The asphere has two terms (4th and 6th order) and ≈ 50 μm of departure.

The full optical path from the sodium layer, through TMT and NFIRAOS, and through the lenslet and relay to the detector, has been modeled. The images from the top and bottom of the sodium layer are easily resolved in the model. The glasses chosen for this design are all highly transmissive in the visible spectrum, with a bulk absorption of $<1\%$. The overall throughput will therefore depend on the quality of the coatings. As in HARMONI, NFIRAOS plans to use high performance monochromatic dielectric coatings.

6 Conclusion

We have evaluated the performance of a CMOS sensor compatible with the current requirements of wavefront sensor of laser guide stars in the context of extremely large telescopes.

We have shown that the read-out noise of $\approx$3 e^- is achievable for a large sensor array. The statistical distribution of read-out noise over the sensor shows a tailed shape which is characteristic of CMOS sensors. The impact of this read-out noise excess in the centroid estimation accounts for a factor of <2 above 500 photons/sub-aperture/frame.

The average angular response of the sensor was characterized showing a two-axes symmetry with full width half maximum of 42.6° in the vertical direction and 25.4° in the horizontal direction. The angle of acceptance leads to a light transmission loss depending of the beam aperture on the sensor. For a square lenslet, a drop of 10% in transmission is found for a beam focal ratio on the detector of $F_d = 2.5$. We provide the calculated transmission curves for circular and square lenslet shapes as a reference for wavefront sensor designers using this type of detectors.

The error of center of gravity was employed as a metric to evaluate the performance of the detector to wavefront sensing. We simulated and measured the CoG errors as a function of the photon flux and found a good agreement between theory and experimental results. The centroiding linearity was measured for different spot size and angles of incidence. The rising of non-linearities in the estimation of the CoG is in agreement with our simulations and shows that for a sampling frequency of 1.36 pixel per FWHM (Nyquist undersampled), the degree of non-linearities is 1.0% of a pixel.

Finally, we show two examples of practical implementations of this detector in LGS wavefront sensors for ESO ELT/HARMONI and TMT/NFIRAOS adaptive optics systems. The need of additional relay optics between the microlens array and the detector is common in both cases due to the differences in size between the CMOS sensor and the pupil. Moreover, the telecentric double-sided lenslet array in the HARMONI design, also adopted in NFIRAOS, comes as an innovative solution to achieve the required sub-aperture FoV despite the CMOS architecture intrinsically limiting the acceptance angle into the pixels. In the case of NFIRAOS, only a sub-region of the detector needs to be read, which allows operating at higher frame rate, as well as greatly relaxing key opto-mechanical tolerances. For HARMONI, a larger LGS elongation is expected and all pixels of the detector are needed to accommodate a larger sub-aperture FoV that minimizes truncation over most of the pupil. These two examples show that this type of detector is very suitable for LGS wavefront sensing on extremely large telescopes.

Acknowledgments

Z.K. acknowledges financial support from China Scholarship Council award no. 201806010330. This project received funding from the European Union's Horizon 2020 research and innovation programme under the Marie Sklodowska-Curie grant agreement No 893150. This work also benefited from the support of the WOLF project ANR-18-CE31-0018 of the French National Research Agency (ANR). This document has been prepared as part of the activities of OPTICON H2020 (2017-2020) Work Package 1 (Calibration and test tools for AO assisted E-ELT instruments). OPTICON is supported by the Horizon 2020 Framework Programme of the European Commission's (Grant number 730890). This work was supported by the Action Spécifique Haute Résolution Angulaire (ASHRA) of CNRS/INSU co-funded by CNES. This work has been partially supported by the LabEx FOCUS ANR-11-LABX-0013

References

1 G. A. Hawker and I. R. Parry, "High-resolution spectroscopy and high contrast imaging with the ELT: looking for O_2 in Proxima b," *Monthly Notices of the Royal Astronomical Society* **484**, 4855–4864 (2019).

2 B. García-Lorenzo, A. Monreal-Ibero, E. Mediavilla, *et al.*, "Black hole-galaxy scaling relation evolution from Z$\sim$2.5: Simulated observations with HARMONI on the ELT," *Frontiers in Astronomy and Space Sciences* **6**, 73 (2019).

3 H. Bonnet, F. Biancat-Marchet, M. Dimmler, *et al.*, "Adaptive optics at the ESO ELT," in *Adaptive Optics Systems VI*, L. M. Close, L. Schreiber, and D. Schmidt, Eds., **10703**, 327 – 335, International Society for Optics and Photonics, SPIE (2018).

4 W. Happer, G. J. MacDonald, C. E. Max, *et al.*, "Atmospheric-turbulence compensation by resonant optical backscattering from the sodium layer in the upper atmosphere," *J. Opt. Soc. Am. A* **11**, 263–276 (1994).

5 C. A. Primmerman, D. V. Murphy, D. A. Page, *et al.*, "Compensation of atmospheric optical distortion using a synthetic beacon," *Nature* **353**, 141–143 (1991).

6 E. Vernet-Viard, F. Delplancke, N. N. Hubin, *et al.*, "LGS Na spot elongation and Rayleigh scattering effects on Shack-Hartmann wavefront sensor performances," in *Adaptive Optics Systems and Technology*, R. K. Tyson and R. Q. Fugate, Eds., **3762**, 8 – 19, International Society for Optics and Photonics, SPIE (1999).

7 S. J. Thomas, S. Adkins, D. Gavel, *et al.*, "Study of optimal wavefront sensing with elongated laser guide stars," *Monthly Notices of the Royal Astronomical Society* **387**, 173–187 (2008).

8 R. M. Clare, S. J. Weddell, and M. Le Louarn, "Mitigation of truncation effects in elongated Shack-Hartmann laser guide star wavefront sensor images," *Applied Optics* **59**, 6431 (2020).

9 L. Schreiber, M. Lombini, I. Foppiani, *et al.*, "An optical solution to the LGS spot elongation problem," in *Adaptive Optics Systems*, N. Hubin, C. E. Max, and P. L. Wizinowich, Eds., *Society of Photo-Optical Instrumentation Engineers (SPIE) Conference Series* **7015**, 70151O (2008).

10 A. G. Basden, L. Bardou, D. Bonaccini Calia, *et al.*, "On-sky demonstration of matched filters for wavefront measurements using ELT-scale elongated laser guide stars," *Monthly Notices of the Royal Astronomical Society* **466**, 5003–5010 (2017).

11 A. Berdja, E. Garcés Santibañez, and C. D. Guzmán, "Experimental results on using artificial neural networks for accurate centroiding in Shack-Hartmann wavefront sensors with elongated spots," in *Adaptive Optics Systems V*, E. Marchetti, L. M. Close, and J.-P. Véran, Eds., *Society of Photo-Optical Instrumentation Engineers (SPIE) Conference Series* **9909**, 99093Y (2016).

12 C. Béchet, M. Tallon, I. Tallon-Bosc, *et al.*, "Optimal reconstruction for closed-loop ground-layer adaptive optics with elongated spots," *J. Opt. Soc. Am. A* **27**, A1–A8 (2010).

13 E. N. Ribak and R. Ragazzoni, "Reduction of laser spot elongation in adaptive optics," *Optics Letters* **29**, 1351–1353 (2004).

14 L. Gilles and B. Ellerbroek, "Shack-Hartmann wavefront sensing with elongated sodium laser beacons: centroiding versus matched filtering," *Applied Optics* **45**, 6568–6576 (2006).

15 S. Oberti, J. Kolb, P.-Y. Madec, *et al.*, "The AO in AOF," in *Adaptive Optics Systems VI*, L. M. Close, L. Schreiber, and D. Schmidt, Eds., *Society of Photo-Optical Instrumentation Engineers (SPIE) Conference Series* **10703**, 107031G (2018).

16 W. Hackenberg, D. Bonaccini Calia, B. Buzzoni, *et al.*, "ESO 4LGSF: Integration in the VLT, Commissioning and on-sky results," in *Adaptive Optics Systems VI*, *Society of Photo-Optical Instrumentation Engineers (SPIE) Conference Series* **9909** (2016).

17 J. W. Beletic, S. Adkins, B. Burke, *et al.*, "The Ultimate CCD for Laser Guide Star Wavefront Sensing on Extremely Large Telescopes," *Experimental Astronomy* **19**, 103–109 (2005).

18 M. Downing, M. Casali, G. Finger, *et al.*, "AO WFS detector developments at ESO to prepare for the E-ELT," in *Adaptive Optics Systems V*, E. Marchetti, L. M. Close, and J.-P. Véran, Eds., *Society of Photo-Optical Instrumentation Engineers (SPIE) Conference Series* **9909**, 990914 (2016).

19 M. Downing, P. Amico, M. Brinkmann, *et al.*, "Update on development of WFS cameras at ESO for the ELT," in *Adaptive Optics Systems VI*, L. M. Close, L. Schreiber, and D. Schmidt, Eds., *Society of Photo-Optical Instrumentation Engineers (SPIE) Conference Series* **10703**, 107031W (2018).

20 E. R. Fossum, "Active pixel sensor array with electronic shuttering," *US patent 6,486,503* (1997).

21 K. Yasutomi, S. Itoh, S. Kawahito, *et al.*, "Two-stage charge transfer pixel using pinned diodes for low-noise global shutter imaging," in *International Image Sensor Society Workshop*, (2009).

22 T. Inoue, S. Takeuchi, and S. Kawahito, "CMOS active pixel image sensor with in-pixel CDS for high-speed cameras," in *Sensors and Camera Systems for Scientific, Industrial, and Digital Photography Applications V*, N. Sampat, R. J. Motta, and M. M. Blouke, Eds., **5301**, 250 – 257, International Society for Optics and Photonics, SPIE (2004).

23 R. Zhang and L. Lai, "Optical design of microlens array for CMOS image sensors," in *8th International Symposium on Advanced Optical Manufacturing and Testing Technologies: Design, Manufacturing, and Testing of Micro- and Nano-Optical Devices and Systems; and Smart Structures and Materials*, X. Luo, T. Ye, T. Xin, *et al.*, Eds., **9685**, 1 – 7, International Society for Optics and Photonics, SPIE (2016).

24 M. Downing, J. Kolb, D. Baade, *et al.*, "Backside-illuminated, high-QE, 3e- RoN, fast 700fps, 1760x1680 pixels CMOS imager for AO with highly parallel readout," in *High Energy, Optical, and Infrared Detectors for Astronomy V*, A. D. Holland and J. W. Beletic, Eds., *Society of Photo-Optical Instrumentation Engineers (SPIE) Conference Series* **8453**, 84530C (2012).

25 M. Downing, J. Kolb, B. Dierickx, *et al.*, "LGSD/NGSD: high speed visible CMOS imagers for E-ELT adaptive optics," in *High Energy, Optical, and Infrared Detectors for Astronomy VII*, A. D. Holland and J. Beletic, Eds., **9915**, 401 – 408, International Society for Optics and Photonics, SPIE (2016).

26 E. R. Fossum and D. B. Hondongwa, "A review of the pinned photodiode for ccd and cmos image sensors," *IEEE Journal of the Electron Devices Society* **2**(3), 33–43 (2014).

27 M. Guidash, J. Ma, T. Vogelsang, *et al.*, "Reduction of cmos image sensor read noise to enable photon counting," *Sensors* **16**(4) (2016).

28 P. Jerram, D. Burt, N. Guyatt, *et al.*, "Back-thinned CMOS sensor optimization," in *Optical Components and Materials VII*, S. Jiang, M. J. F. Digonnet, J. W. Glesener, *et al.*, Eds., **7598**, 298 – 309, International Society for Optics and Photonics, SPIE (2010).

29 J.-L. Gach, D. Boutolleau, C. Brun, *et al.*, "C-BLUE One: a new CMOS camera dedicated for laser guide star wavefront sensing on ELTs," in *Adaptive Optics Systems VII*, L. Schreiber, D. Schmidt, and E. Vernet, Eds., **11448**, International Society for Optics and Photonics, SPIE (2020).
30 J. R. Janesick, *Photon Transfer*, vol. PM170, SPIE press (2007).
31 X. Wang, P. R. Rao, A. Mierop, *et al.*, "Random telegraph signal in cmos image sensor pixels," in *2006 International Electron Devices Meeting*, 1–4 (2006).
32 P. W. R. Connolly, X. Ren, A. McCarthy, *et al.*, "High concentration factor diffractive microlenses integrated with cmos single-photon avalanche diode detector arrays for fill-factor improvement," *Appl. Opt.* **59**, 4488–4498 (2020).
33 S. Gousset, C. Petit, V. Michau, *et al.*, "Modeling of high-precision wavefront sensing with new generation of cmt avalanche photodiode infrared detectors," *Appl. Opt.* **54**, 10163–10176 (2015).
34 N. Muller, *Analyse de front d'onde sur étoiles laser pour les extremely large telescopes*. PhD thesis, Université Paris Diderot (2011). Thèse de doctorat dirigée par Rousset, Gérard et Michau, Vincent Astronomie et astrophysique Paris 7 2011.
35 M. Nicolle, T. Fusco, G. Rousset, *et al.*, "Improvement of shack–hartmann wave-front sensor measurement for extreme adaptive optics," *Opt. Lett.* **29**, 2743–2745 (2004).
36 J. G. Robertson, "Detector Sampling of Optical/IR Spectra: How Many Pixels per FWHM?," *Publications of the Astronomical Society of Australia* **34**, e035 (2017).
37 M. Estribeau and P. Magnan, "CMOS pixels crosstalk mapping and its influence on measurements accuracy in space applications," in *Sensors, Systems, and Next-Generation Satellites IX*, R. Meynart, S. P. Neeck, and H. Shimoda, Eds., **5978**, 315 – 326, International Society for Optics and Photonics, SPIE (2005).
38 N. A. Thatte, I. Bryson, F. Clarke, *et al.*, "HARMONI: first light spectroscopy for the ELT: instrument final design and quantitative performance predictions," in *Ground-based and Airborne Instrumentation for Astronomy VIII*, C. J. Evans, J. J. Bryant, and K. Motohara, Eds., **11447**, 415 – 425, International Society for Optics and Photonics, SPIE (2020).
39 J. Crane, G. Herriot, D. Andersen, *et al.*, "NFIRAOS adaptive optics for the Thirty Meter Telescope," in *Adaptive Optics Systems VI*, L. M. Close, L. Schreiber, and D. Schmidt, Eds., **10703**, 1094 – 1106, International Society for Optics and Photonics, SPIE (2018).

Zibo Ke is a postdoctoral fellow at Chengdu Institute of Optoelectronics, Chinese Academy of Sciences. He is specialized in optics, wavefront sensing, laser guide star, instrumentation in adaptive optics. He holds a PhD in Astrophysics from Aix-Marseille University and has worked on the laser guide star sensors of HARMONI.
Felipe Pedreros Bustos is a *Marie Sklodowska-Curie* Postdoctoral Fellow at the Laboratoire d'Astrophysique de Marseille. His current research is focused on laser guide star physics, wavefront sensing, and instrumentation in adaptive optics. He obtained a PhD in Physics from University of Mainz in 2019 and a Telecommunications Engineering Degree from University of Concepción in 2011.
Jenny Atwood is an Optical Engineer at the National Research Council Canada (NRC), and the lead optical engineer for NFIRAOS for TMT. She has varied experience, from astronomical instrumentation to semi-conductor equipment to high powered laser systems, and her skills are currently

focused on designing and building optical systems for ground-based telescopes around the world. She holds a MS in Optics from the University of Rochester and BA in Physics from Colorado College.

Anne Costille is a permanent staff research engineer at Laboratoire d'Astrophysique de Marseille, currently the systems engineer for the laser guide star sensors of HARMONI, first light instrument of the ESO ELT. She is an engineer specialized in optics and works on the design, assembly and verification of ground or space instruments for astronomy. She hold a PhD in Astrophysics from Paris Diderot University and has worked on the laser tomography adaptive optics.

Kjetil Dohlen is Head of the Optics Department at Laboratoire d'Astrophysique de Marseille (France). Having received his PhD in Applied Optics at Imperial College in 1994, he worked as optical architect for the Rosetta narrow-angle camera (OSIRIS-NAC) and the SPIRE instrument for Herschel, two major European space missions. In 2004 he took on the task of System Engineer for the SPHERE instrument, the extreme AO high-contrast imager for the VLT

Kacem El Hadi graduated from the University of Nice with a PhD in non-linear and integrated optics. He has worked for many years in the field of optical, laser and fiber instrumentation. At the Laboratoire d'Astrophysique de Marseille, he has contributed to the development of different R&D activities (adaptive optics, micro-optics, active optics,) as well as spatial and ground projects. Currently, he is involved in ESO ELT projects at LAM for management and AIT activities.

Jean-Luc Gach is a permanent staff research engineer at the Laboratoire d'Astrophysique de Marseille. His research is oriented on novel detector and focal plane array technologies in the visible and infrared, as well as 3D spectroscopy. He holds a PhD in Instrumentation from Aix-Marseille University, MSc in imagery from Nice University and an Master's Degree of engineering in electronics and signal processing from INSA Lyon.

Glen Herriot is the Systems Engineer for TMT NFIRAOS, being designed at the National Research Council of Canada's Herzberg Astronomy and Astrophysics research centre in Victoria, Canada. He has a degree in Systems Design Engineering from the University of Waterloo, and has developed precision high-resolution instrumentation for more than 15 years in industry, and nearly 30 years at HAA.

Pierre Jouve is a Research Engineer currently working on the HARMONI LGSS prototype at Laboratoire d'Astrophysique de Marseille. He is specialized in optics, wavefront sensing, laser guide star, instrumentation in adaptive optics. He holds a PhD in Quantum Optics from Nottingham University (UK) on the creation of molecular Bose-Einstein condensate.

Lianqi Wang is the adaptive optics systems engineer at TMT, responsible for AO systems performance modeling and wavefront error budget. He is the author of multithreaded adaptive optics simulator (MAOS), a GPU accelerated general purpose AO simulation software. He joined TMT in 2007 after earning his PhD in Physics in University of California, Irvine.

Thierry Fusco is the scientific deputy director of ONERA Optics Department. He has 25 years of expertise in Adaptive Optics and post-processing for astronomy. After a PhD in 2000 on the mitigation of partial correction and anisoplanatism in AO, he was the VLT-SPHERE AO scientist (extreme AO system for direct detection and characterization of extrasolar planet) from 2004 to 2015 and he is now the AO scientist of HARMONI (which gathers both a classical and Laser Tomographic AO system) the first light Integral Field Spectrograph instrument for the European ELT.

Benoit Neichel is a scientist at Laboratoire d'Astrophysique de Marseille, specialist in Adaptive Optics (AO). He got his PhD in 2008, on the definition of AO systems for Extremely Large

Telescopes. Then worked at Gemini-South as Instrument Scientist for the GeMS, the first Multi-Conjugate AO system offered to the community. And today he acts as deputy-PI for HARMONI, the first light Integral Field Spectrograph instrument for the European ELT, assisted by Laser Tomography AO.

Biographies of other authors are not available.